



Numerical Simulation on the Propagation and Deflection of Fast Coronal Mass Ejections (CMEs) Interacting with a Corotating Interaction Region in Interplanetary Space

Yousheng Liu^{1,2}, Fang Shen^{1,2,3} , and Yi Yang^{1,2}¹ SIGMA Weather Group, State Key Laboratory of Space Weather, National Space Science Center, Chinese Academy of Sciences, Beijing, 100190, People's Republic of China; fshen@spaceweather.ac.cn² College of Earth Sciences, University of Chinese Academy of Sciences, Beijing, 100049, People's Republic of China³ Institute of Space Science and Applied Technology, Shenzhen, 518055, People's Republic of China

Received 2019 October 10; revised 2019 November 1; accepted 2019 November 3; published 2019 December 17

Abstract

Previous research has shown that the deflection of coronal mass ejections (CMEs) in interplanetary space, especially fast CMEs, is a common phenomenon. The deflection caused by the interaction with background solar wind is an important factor to determine whether CMEs could hit Earth or not. As the Sun rotates, there will be interactions between solar wind flows with different speeds. When faster solar wind runs into slower solar wind ahead, it will form a compressive area corotating with the Sun, which is called a corotating interaction region (CIR). These compression regions always have a higher density than the common background solar wind. When interacting with CME, will this make a difference in the deflection process of CME? In this research, first, a three-dimensional (3D) flux-rope CME initialization model is established based on the graduated cylindrical shell (GCS) model. Then this CME model is introduced into the background solar wind, which is obtained using a 3D IN (Interplanetary) -TVD-MHD model. The Carrington Rotation (CR) 2154 is selected as an example to simulate the propagation and deflection of fast CME when it interacts with background solar wind, especially with the CIR structure. The simulation results show that: (1) the fast CME will deflect eastward when it propagates into the background solar wind without the CIR; (2) when the fast CME hits the CIR on its west side, it will also deflect eastward, and the deflection angle will increase compared with the situation without CIR.

Unified Astronomy Thesaurus concepts: [Solar coronal mass ejections \(310\)](#); [Corotating streams \(314\)](#); [Solar wind \(1534\)](#); [Magnetohydrodynamical simulations \(1966\)](#)

1. Introduction

Coronal mass ejection (CME) is a phenomenon caused by intense solar activity that erupts a huge amount of plasma and magnetic flux from the corona in a short time. A CME will destroy the steady flow of solar wind when it enters interplanetary space. It is considered to be the main source of disastrous space weather phenomena such as the geomagnetic storm, when the CME hits Earth (Gosling et al. 1990). It has been generally believed that the CMEs, which erupt toward Earth from the solar source regions, will travel along the Sun–Earth line and reach Earth (Howard et al. 1982). However, only a part of such CMEs arrive at Earth and get observed. On the other hand, some CME events that are not erupting in the face of Earth are found to reach Earth (Wang et al. 2004).

The CME deflection was proposed as a probable reason to explain the phenomena above. After erupting from the Sun, a CME can be deflected from its original direction for many reasons. One of the reasons is the effect of the corona, where the magnetic field dominates the dynamic process. The asymmetry of magnetic field structure can make the CME deflect, which has been proven and widely studied (e.g., Gui et al. 2011; Shen et al. 2011a; Wang et al. 2011; Zhou & Feng 2013; Kay et al. 2015, 2016). Another kind of possible deflection occurs in the interplanetary when the CME interacts with other structures. A typical example is the effect of other CMEs (Gopalswamy et al. 2001; Lugaz et al. 2012; Shen et al.

2012a). Moreover, a single CME in interplanetary space may also be deflected due to the influence of the background solar wind (e.g., Wang et al. 2004, 2014). And this kind of kinetic model for CME deflection in the interplanetary space (DIPS) was put forward by the study of Wang et al. (2004), which suggested that a fast CME would always be blocked by the background solar wind and deflected to the east, while a slow one would be pushed and deflected to the west when propagating in the interplanetary space freely. The background mass and magnetic field will accumulate at the leading flow, which makes the total pressure rise in the west front of CME and finally causes the deflection. Manchester et al. (2017) mentioned both the CME deflection in the corona and in the heliosphere, and attributed this to two primary causes: magnetic forces produced by the background corona and the background solar wind flow pattern.

In order to study the CME deflection more effectively and gain more useful information, we can use magnetohydrodynamic (MHD) modeling as a feasible and efficient method. The propagation of CME and its driven shock in the heliosphere have been studied by some researchers using MHD simulation (e.g., Manchester et al. 2004b; Lugaz et al. 2005; Chané et al. 2006; Shen et al. 2014). Furthermore, the deflection and interaction of CMEs also have been studied by MHD modeling. For instance, Zhou & Feng (2017) have shown the CME deflection caused by the influence of heliospheric current sheet (HCS) using a 3D MHD model. Their research suggests that CMEs tend to deflect to the HCS in the latitudinal direction near the Sun and then propagate almost parallel to the HCS in the interplanetary space. Lugaz et al. (2005) has simulated the interaction of two CMEs from the Sun



Original content from this work may be used under the terms of the [Creative Commons Attribution 3.0 licence](#). Any further distribution of this work must maintain attribution to the author(s) and the title of the work, journal citation and DOI.

to Earth, including their magnetic structure, density, energetics, and kinematics in the interplanetary space. Shiota & Kataoka (2016) simulated a series of CMEs with internal spheromak-type magnetic fields. They discovered that one of the CMEs is strongly deflected by the inhomogeneous background solar wind caused by other CMEs that erupted before. Similar research on the interplanetary coupling between multiple magnetic clouds (MCs)/CMEs has been numerically studied by Xiong et al. (2007, 2009), including direct collision and oblique collision. Shen et al. (2011b, 2012b, 2013) also studied the collision and interaction between two CMEs in the heliosphere with a 3D time-dependent numerical MHD model.

When simulating CME propagation, it is very important to choose a suitable CME initialization model. In previous years, the cone model was widely used. This model represents CME as a hydrodynamic pulse of velocity (e.g., Odstrcil & Pizzo 1999). The problem with the cone model is that it does not contain a description of the magnetic field of CME. The plasma blob model proposed by Chané et al. (2005) has also been used by many authors (e.g., Shen et al. 2014). Although this is an extremely simple model describing the CME as a plasma blob with high density, high velocity, and high pressure, it is magnetized with an initial magnetic field. Additionally, a kind of spheromak CME model was developed and studied by several research groups (e.g., Vandas et al. 1997, 1998, 2002; Gibson & Low 1998; Manchester et al. 2004a, 2004b, 2014a, 2014b; Lugaz et al. 2005). This kind of model is characterized by its special magnetic field structure, which is described as a spirally twisted toroidal flux rope confined within a sphere. In this work, we try to introduce the graduated cylindrical shell (GCS) model into our MHD simulation acting as the CME initialization model. The GCS model is an empirical model presented by Thernisien et al. (2006) to describe the flux-rope structure of some CMEs. The model contains a 3D flux-rope morphological structure and expands in a self-similar form. The GCS model is also called a “hollow croissant” because of its characteristic shape: it looks like a curved tubular shell with two thin ends and a thick middle. It has been frequently used to study the morphology, position, and kinematics of CMEs in the coronagraph observation (e.g., Liu et al. 2010; Lynch et al. 2010; Poomvises et al. 2010; Patsourakos et al. 2010).

A corotating interaction region (CIR) is the result of spatial variability in coronal expansion and solar rotation. There are solar wind flows of different speeds in the interplanetary space. When fast solar wind catches up with slow solar wind ahead, it will form a compressive interaction region where the density of particles is increased at the front and relatively sparse at the rear. If this kind of regions are roughly time-stationary and corotate with the Sun, then they will be called the CIRs (Gosling & Pizzo 1999). Compared with the common background solar wind, CIR has lower velocity and higher particle density. Because of its specificity, the interaction between CME and CIR may be different from that between CME and general background solar wind. Although a lot of works related to the CME deflection have been done at present as mentioned above, there are still few researches which focus on the CME deflection caused by CIR. The main reason may be the lack of direct observation and research related to CIR. So in this work, we will try to make a preliminary study of the interaction between them through numerical simulation.

In Section 2, we give a brief introduction of our simulation method, including the ideal MHD equations, grid system, and boundary conditions. The three-dimensional (3D) flux-rope CME initialization model based on the GCS model will also be introduced in this section. The result of our simulation is given in Section 3, as well as the analyses. In Section 4 we summarize the paper and provide a discussion.

2. Numerical Simulation Method

2.1. Background Solar Wind

In order to study the propagation and deflection of the CME in the ambient solar wind, a 3D solar wind background is needed. We construct the solar wind background by solving the ideal MHD equations with the TVD-Lax–Friedrichs (TVD-LF) scheme. The ideal MHD equations in a rotating spherical coordinate system (r, θ, ϕ) can be written as

$$\frac{\partial \rho}{\partial t} + \nabla \cdot (\rho \mathbf{V}) = 0 \quad (1)$$

$$\begin{aligned} \frac{\partial \rho \mathbf{v}}{\partial t} + \nabla \cdot \left[\left(p + \frac{B^2}{2\mu_0} \right) \vec{I} + \rho \mathbf{V} \mathbf{V} - \frac{\mathbf{B} \mathbf{B}}{\mu_0} \right] \\ = -\frac{\rho G M_s \mathbf{r}}{r^2} + \mathbf{f} \end{aligned} \quad (2)$$

$$\frac{\partial \mathbf{B}}{\partial t} + \nabla \cdot (\mathbf{V} \mathbf{B} - \mathbf{B} \mathbf{V}) = 0 \quad (3)$$

$$\frac{\partial p}{\partial t} + \nabla \cdot (\rho \mathbf{V}) + (\gamma - 1) p \nabla \cdot \mathbf{V} = 0 \quad (4)$$

where ρ , \mathbf{V} , p stand for density, velocity and pressure of the plasma, respectively; \mathbf{B} stands for the magnetic field vector; \vec{I} is the unit tensor; M_s is the mass of the Sun; $\mathbf{f} = -[\boldsymbol{\omega} \times (\boldsymbol{\omega} \times \mathbf{r}) + 2\boldsymbol{\omega} \times \mathbf{V}]$ is the centrifugal force in the rotating coordinate system and $\boldsymbol{\omega} = 2\pi/T$, where the T represents the solar rotation period of 24.47 days (Shen et al. 2018).

The computational domain covers $21.5R_s \leq r \leq 244R_s$, $-90^\circ \leq \theta \leq 90^\circ$ and $0^\circ \leq \phi \leq 360^\circ$. Here the grid mesh is built in the form of $224(r) \times 180(\theta) \times 360(\phi)$. The mesh is uniform in the longitudinal and latitudinal directions with $\Delta\theta = 1^\circ$ and $\Delta\phi = 1^\circ$; in the radial direction, the grid size gradually varies from about $0.37R_s$ at the inner boundary of $21.5R_s$ to $2.28R_s$ at the outer boundary near 1 au. Compared with the common spherical coordinate mesh system, here we use a more complicated mesh system that is composed of six component meshes (Feng et al. 2010). The six components are identical and partially overlap on their boundary to form a complete sphere. The main reason for using this mesh system is to avoid the problem of computational efficiency decline caused by the coordinate singularity of the polar region.

The Carrington Rotation (CR) 2154 is chosen for background establishment. In this CR, there are three obvious CIRs on the ecliptic plane and the distance between two of them is relatively large. When a CME is propagating in the region between the two CIRs, it can be influenced by only one of them. This is convenient for us to observe and study.

First, we use the potential field source surface (PFSS) model to extrapolate the coronal magnetic field from the photospheric magnetic field provided by the Global Oscillation Network Group (GONG) project. Actually, we do not calculate the

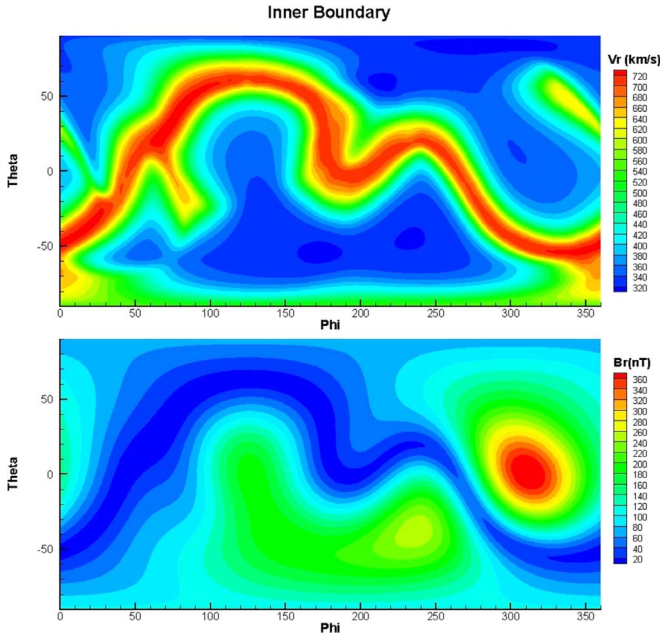


Figure 1. Radial velocity distribution based on the WSA model (top) and the radial magnetic field distribution according to the PFSS model (bottom) on the inner boundary.

coronal region in the simulation of background solar wind because the inner boundary of our model is set at 0.1 au from the solar center. Here we calculate the coronal magnetic field to obtain the parameters f_s and θ_b on the source surface, which are necessary configuration parameters of our model. f_s is the expansion factor, which is defined as:

$$f_s = \left(\frac{B_s}{B_{ss}} \right) \left(\frac{R_s}{R_{ss}} \right)^2 \quad (5)$$

where B_s and B_{ss} are the magnetic field strength on the photosphere and on the source surface, respectively; R_s and R_{ss} are the radius of the Sun and of the source surface, respectively. θ_b is the minimum angular distance from the footpoint of the magnetic field line at the Sun's surface to the nearest coronal hole boundary.

Then we can initialize the distribution of the solar wind velocity at the inner boundary ($21.5R_s$) with the distribution of f_s and θ_b on the source surface according to the Wang–Sheeley–Arge (WSA) empirical model. The empirical formula of the WSA model can be written as (Arge et al. 2003):

$$V_r = V_s + \frac{V_f}{(1 + f_s)^{a_1}} \left[1 - 0.8 \cdot \exp \left\{ - \left(\frac{\theta_b}{a_2} \right)^{a_3} \right\} \right]^{a_4} \quad (6)$$

where V_s means the slowest solar wind speed and V_f is the fastest speed; a_1 to a_4 are free parameters to adjust the solar wind speed in the model. The velocities in the longitudinal and latitudinal directions (V_ϕ and V_θ) are assumed to be zero. There are eight free parameters, including V_s , V_f , a_1 to a_4 , f_s and θ_b , which can be adjusted to set different inner boundary conditions for different periods (Shen et al. 2018). Figure 1 shows the distributions of radial velocity and radial magnetic field strength on the inner boundary during CR 2154 that we have built. The inner boundary is given in a fixed way that depends only on the initial parameters and does not change

with time; the outer boundary satisfies the nonreflecting boundary condition.

In order to avoid the numerical reconnection of the interplanetary magnetic field in the simulation, we only retain the intensity of the magnetic field and set the direction of all the magnetic fields in the positive direction when we initialize the interplanetary magnetic field, namely, all the magnetic lines are directed outward. This approach should be reasonable because even if we retain the positive and negative polarities of the interplanetary magnetic field, we can still select the regions with the unidirectional magnetic field for simulation experiments.

To avoid the accumulation of the $\nabla \cdot \mathbf{B}$ error and keep the physical law of $\nabla \cdot \mathbf{B} = 0$ during the calculation, here we use a diffusive approach to control it. The $\nabla \cdot \mathbf{B}$ error can be diffused away by iterating as follows at each timestep:

$$\mathbf{B}^{n+1} = \mathbf{B}^n + \mu (\Delta x)^2 \nabla \nabla \cdot \mathbf{B}^n \quad (7)$$

where

$$(\Delta x)^2 = \frac{1}{\frac{1}{(\Delta r)^2} + \frac{1}{(r \Delta \theta)^2} + \frac{1}{(r \sin \theta \Delta \phi)^2}}$$

in the spherical coordinate system and n is the number of iterations; the value of μ is set to be 0.3 (e.g., Shen et al. 2014, 2018).

2.2. CME Initialization

2.2.1. Geometric Parameter

The GCS model was developed by Thernisien et al. (2006) to describe the 3D shape and structure of CMEs. The model consists of two main parts: two conical legs and a curved front. The schematic of this model is shown in Figure 2(a); the origin O is the vertices of the two conical legs, which is set as the center of the Sun; the bottoms of the two cones are connected with the curved front. The cross section of the model is a group of circular annuli with gradually varying radii. The geometric relationship of the varying radius a could be given by

$$a(r) = \kappa r \quad (8)$$

where r is the distance from a point on the shell to the center of the Sun; κ is called the aspect ratio of the model by Thernisien et al. (2006, 2009). The angle between the axis of two conical legs is 2α and the height of the cone is h . So the model is described in a self-similar way and we can completely define the geometry of the shell with three parameters κ , α , and h .

The geometric parameters of the model can also be fully solved and expressed by κ , α , and h . Arc (C) is a circle arc in the plane (O, x, y) with its center at $B(0, b, 0)$ and its radius $\rho = \overline{BD}$ intersecting the y -axis at A, as shown in Figure 2(b) with the dashed arc line. According to the geometrical relationship:

$$b = h / \cos \alpha \quad (9)$$

$$\rho = h \tan \alpha. \quad (10)$$

The cross section of the shell in the plane (B, \mathbf{BG}, z) according to the definition, where C is the center and R is the radius of the

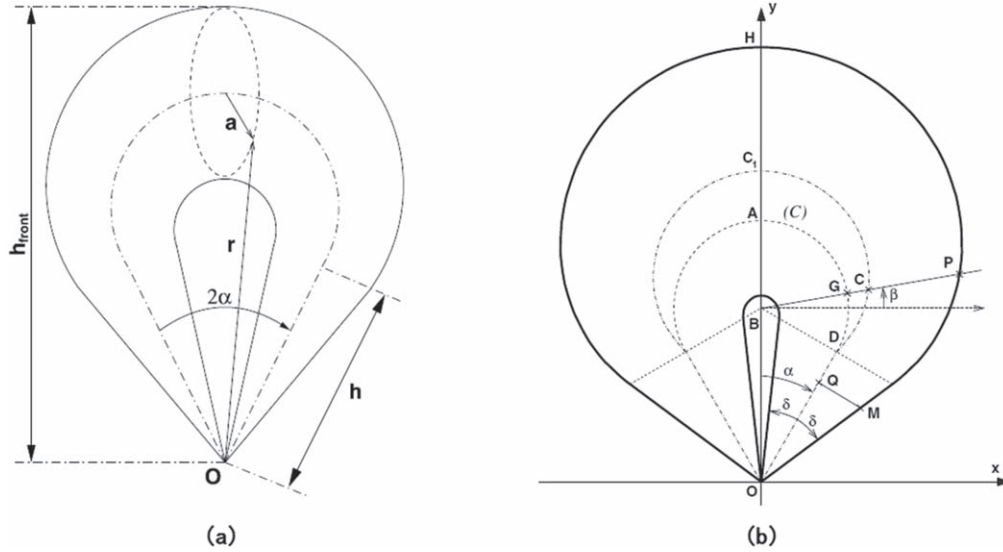


Figure 2. Face-on schematic of the graduated cylindrical shell model. (a): the framework (Figure 1(a) in Thernisien et al. 2009). The dashed–dotted line is the axis of the flux-rope model; the dotted line of a circle is the cross section of the shell model; h_{front} is the height of the whole model. (b): the schematic of the detailed geometric parameter (Figure 1(a) in Thernisien 2011). The dashed circle arc (C) is the generating line of the front part of the model; the dashed–dotted line above is the trajectory of the centers of the model sections, and the point C is both on this trajectory and on the same line with the vector \mathbf{BG} .

circle. The radius R can be expressed as

$$R^2 = \left(\frac{\rho + b\kappa^2 \sin \beta}{1 - \kappa^2} \right)^2 + \frac{b^2\kappa^2 - \rho^2}{1 - \kappa^2} \quad (11)$$

where β is the angle between vector \mathbf{BG} and x -axis. The detailed deduction can be found in Thernisien (2011).

Since R is a function of parameters h , α , and κ , the geometry of the front part has been defined. Combining with the geometry of conical legs, we can completely define the geometry of the whole GCS model by parameters h , α , and κ . Furthermore, we get the expression of the trajectory of the cross-section centers, which is the axis of the model, which is shown in Figure 2(b) with the dotted arc line.

2.2.2. Physical Parameters

After getting the geometric description of the model, we will discuss about the determination of its physical parameters in this subsection. Here we define the magnetic field distribution of our model based on the flux-rope model that Lundquist proposed (Lundquist 1951). It is a force-free solution given in cylindrical coordinate (r, ϕ, z) as

$$\begin{cases} B_r = 0 \\ B_\phi = \sigma_h B_{\text{max}} J_1(\alpha r) \\ B_z = B_{\text{max}} J_0(\alpha r) \end{cases} \quad (12)$$

where J_1 and J_0 are the first-order and zero-order Bessel function, respectively; $\sigma_h = \pm 1$ is the helicity sign, which stands for the helical direction of the magnetic field; α is the force-free parameter; B_{max} is the maximum of the magnetic field. When $r = 0$, here comes

$$J_0 = 1, J_1 = 0 \quad (13)$$

so the magnetic field intensity reaches the maximum on the axis of the cylinder where $r = 0$. We make a standard assumption that the axial component of the magnetic field comes to be zero at the edge of the flux rope, i.e., the first zero

of J_0 should occur when $r = R$, and R stands for the radius of the cylindrical shell. And easily we can get

$$\alpha R \approx 2.405 \quad (14)$$

as proposed by Dasso et al. (2006); the maximum of magnetic field B_{max} of a Lundquist flux rope is written as

$$B_{\text{max}} = \sqrt{\frac{2.405 H_m}{4\pi L R J}} \quad (15)$$

where

$$J = \int_0^R J_1^2(\alpha r) dr. \quad (16)$$

H_m is the magnetic helicity of the Lundquist flux-rope and L is the flux-rope length, which can be written as

$$L = 2\omega(H_{\text{front}} - R_{\text{front}}) \quad (17)$$

where ω is the half-angular width of the GCS model, and H_{front} and R_{front} are the maximum height and maximum radius of the front.

Here we consider a limiting case of the model. Set $\alpha = \delta$, then the inner sides of the two cones coincide at the y -axis, and there is no gap between the two conical legs. The point B becomes the center of the model, such that the plasma parameters of the CME can be defined around the center B like a plasma blob model (e.g., Chané et al. 2005; Shen et al. 2011b, 2011c, 2012b, 2013); but at the same time, we keep the magnetic field structure as a flux rope. The initial density, velocity, and temperature of the point P in CME are given as follows:

$$\begin{cases} \rho_{\text{cme}} = \rho_{\text{max}} \left(1 - \frac{d^2}{(2r)^2} \right) \\ V_{\text{cme}} = V_{\text{max}} \left(1 - \frac{d^2}{(2r)^2} \right) \\ T_{\text{cme}} = T_{\text{max}} \left(1 - \frac{d^2}{(2r)^2} \right) \end{cases} \quad (18)$$

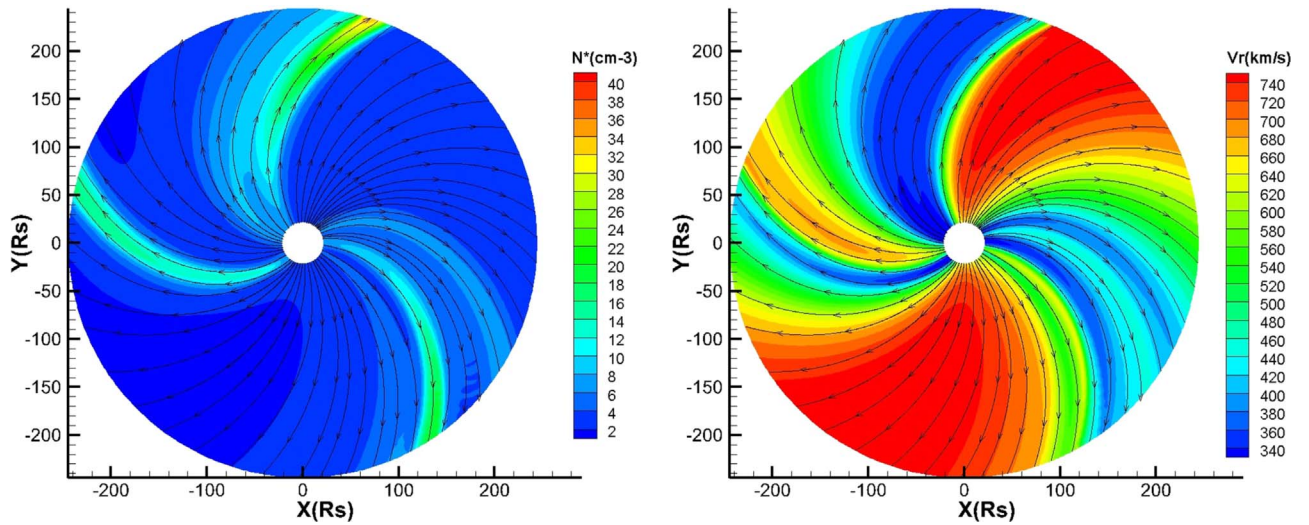


Figure 3. The distribution of density (left) and velocity (right) on the ecliptic plane. The density here is transformed according to the radial distance.

At the front part, r is the radius of the cross section at the point, and d stands for the distance to the center point B ; at the part of the conical legs, r still represents the radius of the cross section, but d is defined as the distance to the inner side of the cone in the cross-section plane. ρ_{\max} , V_{\max} , and T_{\max} are the maximum density, radial velocity, and temperature of the CME.

The total density, radial velocity, and temperature of the CME area can be written as:

$$\begin{cases} \rho_{\text{total}} = \rho_{\text{cme}} + \rho_0 \cdot \frac{d^2}{(2r)^2} \\ V_{\text{total}} = V_{\text{cme}} + V_0 \cdot \frac{d^2}{(2r)^2} \\ T_{\text{total}} = T_{\text{cme}} + T_0 \cdot \frac{d^2}{(2r)^2} \end{cases} \quad (19)$$

where ρ_0 , V_0 , and T_0 stand for the density, radial velocity, and temperature of the background solar wind, respectively.

3. Simulation Results and Analysis

3.1. Propagation and Deflection of the CME

To obtain the steady background used in our simulation we first run the code without initializing the CME. After about 200 hr of the computing time, the physical parameters of the background solar wind do not change anymore and come to a steady state. The distributions of density and velocity on the ecliptic plane in this state are shown in Figure 3. After stabilization, the flow field and magnetic field of the whole background become spiral. We can see three distinct compression regions in Figure 3, where the plasma density is higher and the radial velocity is lower.

With the increase of radial distance, the density of the background solar wind decreases rapidly, such that the density distribution in the whole interplanetary space spans several orders of magnitude. If the density distribution is plotted into a figure directly, the difference of density in the radial direction will be much larger than that in the longitudinal direction. In order to show the compression structure in longitudinal direction better, we need to change the form of the density before we show it in a figure. We transform the density N into

Table 1

Initial Parameters of CME

ρ_{\max} (kg m $^{-3}$)	V_{\max} (km s $^{-1}$)	T_{\max} (K)	H_m (Mx 2)	h (R_s)	α ($^\circ$)	σ ($^\circ$)
1.15×10^{-18}	1200	6×10^6	1.0×10^{42}	25	20	20

N^* in the following way:

$$N^* = N \cdot \left(\frac{r}{215R_s} \right)^2 \quad (20)$$

where r stands for the radial distance. With this method, the attenuation of density due to the increase of radial distance will be reduced and the difference in longitudinal direction will be shown more clearly.

We then start initializing and adding the CME model at the longitude of -40° , where its launch direction will be very close to the CIR. The geometric parameters and the physical parameters of the CME are shown in Table 1. The values of α and δ in the model are set to be equal as mentioned above, so there is no gap between the two conical legs of the CME. The shape of the CME looks like a slightly stretched plasma blob model, in which the distribution of density, velocity, and temperature in the middle part are higher than that near the edge, and the magnetic field of the CME maintains a flux-rope structure. A schematic graph of the magnetic field structure of the initialized CME is shown in Figure 4. The shape of the magnetic field is like a twisted and curved tube.

For convenience, we rotate the whole background around the Z -axis by 40° so that the projection point of CME will always lie in the direction of $\phi = 0$, that is, along the positive direction of the X -axis. This ensures that, no matter what projection angle CME is initialized at, the region of CME propagation is roughly in the same direction, which is convenient for observation and comparison. The image of the propagation process of the CME on the ecliptic plane (plane X - Y) is shown in Figure 5. Since the CME has a much higher speed than the CIR, it soon catches up and hits the CIR on its west side after the propagation starts. At the front of CME's forward direction, there is an obvious shock structure. On the side of their contact, intense compression and interaction occur between them. The

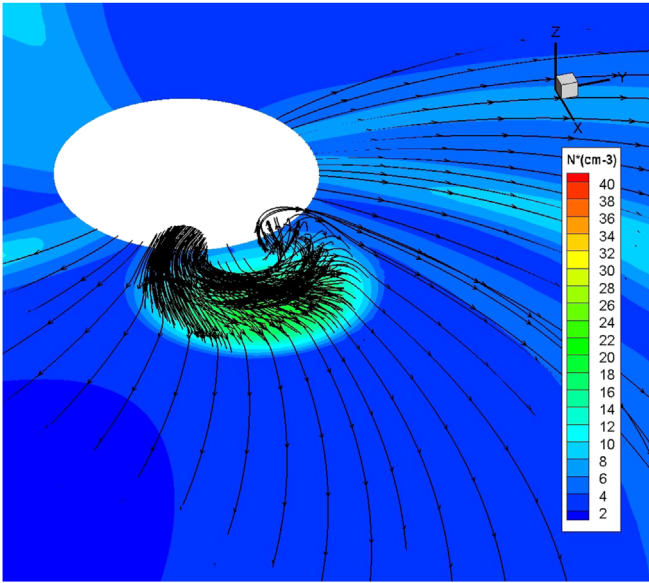


Figure 4. Schematic of the magnetic field structure of the initialized CME at $t = 0$ hr. The background section is the ecliptic plane.

whole process looks like the CME is expanding, moving along the CIR and interacting with it. It can be seen from the three panels on the top of Figure 5, as the CME moves along the CIR, the density of CME increases on its northwest side. This increase is becoming more and more evident over time. Comparing with the three panels on the bottom, the high-speed part of the CME is mainly located on the east side of the high-density part and becomes more and more eastward. Intuitively, it looks like the high-density part of the interaction area makes the direction of the high-speed part of the CME gradually deflect eastward.

Assuming that the CME's initial launched direction is toward Earth, we can see the relationship between the locations of Earth and the CME during the propagation from Figure 5. Figure 6 shows the temporal profiles of plasma parameters at the Earth for 60 hr. This figure shows that the CME arrives at Earth about 29 hr after the CME launches. A sudden change can be seen in the magnetic field intensity, velocity, and density, which means that the shock reaches Earth. Before the shock arrives, there is a period for about 18 hr (shown in gray in Figure 6), in which some parameters start to change. The density slowly rises to a significant peak of about 20 cm^{-3} , and the radial velocity of the solar wind rises from 400 to over 600 km s^{-1} . But these changes are not as sudden as the shock; they are more gradual and gentle. This period indicates the process through which Earth passes through the CIR.

3.2. Determination of CME Location and Direction

Here we determine the CME region using the relative density increment σ , which is defined as

$$\sigma = \frac{\rho - \rho_0}{\rho_0}. \quad (21)$$

ρ_0 is the density of the background solar wind before the CME is added; ρ is the density when the CME is added and propagating. If the σ of a point is larger than 25%, we assume that the point belongs to the CME region. Considering only the data on the ecliptic plane, we can determine a series of points

influenced by CME according to the relative density increment, then the location and direction of the CME can be described numerically with these points.

As mentioned above, the CME spreads outward and expands at the same time during its propagation, so we will give a brief way to describe the position of the whole CME. Observing the shape of the CME from Figure 5, we can see that the CME front is like a part of a circle in the ecliptic plane. Therefore, in this study, we assume the CME to be a circle shape in the 2D graph briefly, and call it the CME circle. A schematic image of the definition of the CME circle is shown in Figure 7.

In order to represent the CME with a circle, we need to know the direction and size of the CME. The CME front is chosen to determine the direction of the CME, and it is defined as: the point in the CME with the largest radial distance from the Sun. To prevent the fluctuation of the coordinates, here we use a set of points instead of just one point to represent the CME front. Therefore, we select the points with the top 20% of the largest heliocentric distance from the sequence of CME points determined by relative density increment, and calculate their coordinates as the following to indicate the position of the CME front:

$$x_f = \frac{\sum_{i=1}^N x_i}{N}, y_f = \frac{\sum_{i=1}^N y_i}{N} \quad (22)$$

where (x_i, y_i) is the coordinates of the selected top 20% of the points, and (x_f, y_f) is the calculated coordinate of the CME front.

Usually, the direction of the CME refers to the longitude direction of its geometric center or the center of mass (e.g., Lugaz et al. 2005; Shen et al. 2011b, 2012b; Shiota & Kataoka 2016; Zhou & Feng 2017). The main reason we do not use these methods to represent the direction of the CME here is to avoid the interference of incorrect statistical methods on the judgment of the deflection. When CME is interacting intensely with CIR, the plasma between them is compressed, and the density of plasma in this area rises. A number of points belonging to the CIR meet the condition of the relative density increment larger than 25%, but in fact they are not a part of the CME. We note that some superfluous and unnecessary points may be counted into the CME in this way. Therefore, errors would occur if all the points that satisfy the relative density increment conditions are used to calculate the position and the direction of the CME. The center of gravity of the CME calculated directly will be closer to the CIR side than its actual location, as well as the propagation direction, which will interfere with our judgment of the deflection of the CME.

Since it is difficult to distinguish the points between CME and CIR only by the relative density increment near the interaction region, we change the way to define the direction and the location of the CME: instead of using all the points, we choose only part of them, which are far from the region of interaction. Furthermore, the choice of CME front as the direction of CME is not only because we cannot use all the points on both sides of CME, but also because it can well represent the direction of CME during the propagation. The point with the greatest distance from the Sun shows that it has the greatest integral of radial velocity during the whole propagation. It can well represent the expansion direction of the CME, that is, the propagation direction of the CME at the moment.

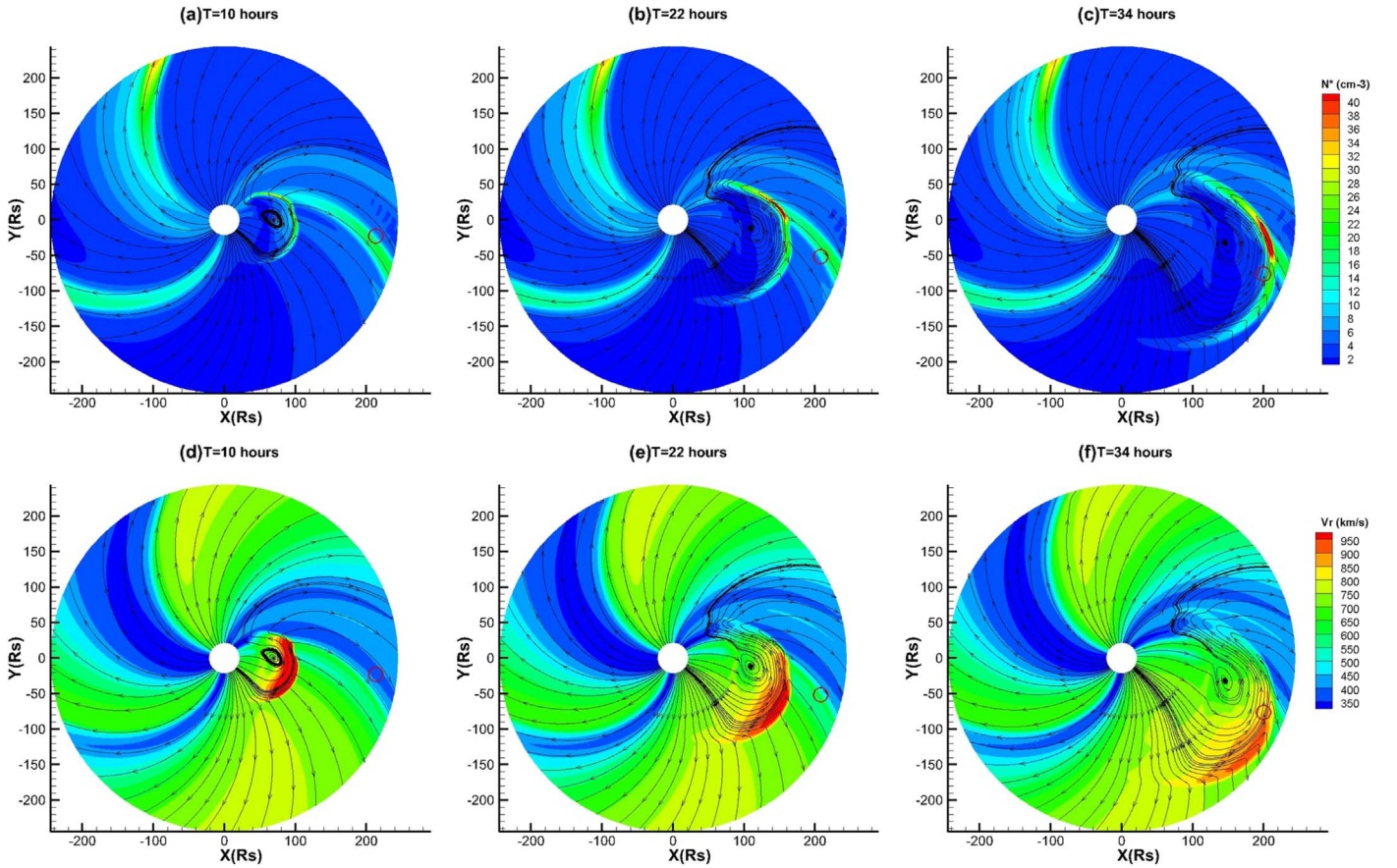


Figure 5. (a)–(c): density distributions on the X – Y plane at different times during the CME propagation. (d)–(f): radial velocity distributions on the X – Y plane. (a) and (d) last occur at 10 hr; (b) and (e) occur at 22 hr; (c) and (f) occur at 34 hr. The small red circle is the position of Earth.

The size of the CME is determined by its front position and the easternmost point. First, connect the CME front that we have defined above with the location of the Sun, i.e., the origin of the coordinate, as represented by the dashed red line \overline{OA} in Figure 7. Then, find the easternmost point of the CME on the ecliptic plane and make a straight line through it from the origin of the coordinate, as represented by the red solid line \overline{OB} in Figure 7. Finally, we can draw a circle that passes point A, with its center lying on \overline{OA} , and make it tangential to the line \overline{OB} at the same time. In this way, the location and the size of the CME are determined by the CME circle.

3.3. Analysis of the Deflection

Using the definition of the CME location and direction mentioned above, the deflection of the CME in the longitudinal direction during the propagation is calculated, as shown in Figure 8(a). When the CME arrives near the Earth, its direction shifts to the east by over 10° . The trajectory of the CME is expressed in Figure 8(c) by a series of CME circles with a time interval of 3 hr.

Although the result of our simulation shows that the CME is deflected significantly, it is important to note that the method we have used to define the deflection is asymmetric. This approach of using only one side of the CME data may lead to systematic errors. Considering this, here we present a comparative example to eliminate system errors. We launch another CME with exactly the same parameters except for its launch position and propagation condition. This CME is

launched at the longitude of -70° , which is in the middle of two CIRs. Since the region between the west and east CIRs is wide enough, this CME will not interact intensely with the CIRs and can almost expand freely during the propagation. Its deflection will be calculated in the same asymmetric way. By comparing the result with the former CME, we can distinguish whether there are obvious systematic errors.

Similarly, we graph the position and direction of the CME circle under this condition in Figure 8(b). Compared with Figure 8(a), we can clearly see that the CME deflection is much smaller under this condition, which is only about 5° near Earth. The trajectory of the CME in this case is shown in Figure 8(d) with the same time interval of 3 hr.

The DIPS model suggests the relationship among the background solar wind speed, the CME speed, and the deflection angle is

$$\Delta\phi(t) = \frac{V_{\text{sw}} - V_r}{V_{\text{sw}}} \Omega t \quad (23)$$

where $\Delta\phi(t)$ is the deflection angle of the CME, V_{sw} is the solar wind speed, and V_r is the CME radial speed; Ω is the rotation speed of the Sun (Wang et al. 2014). The solar wind speed and the CME radial speed here are assumed to be constant. From the velocity distribution in Figure 3, we can take 720 km s^{-1} as the average speed of the solar wind in the CME propagation region. The average radial speed of the CME can be calculated by its total propagation distance and total propagation time. In this case, the propagation distance of the CME is about $165R_s$,

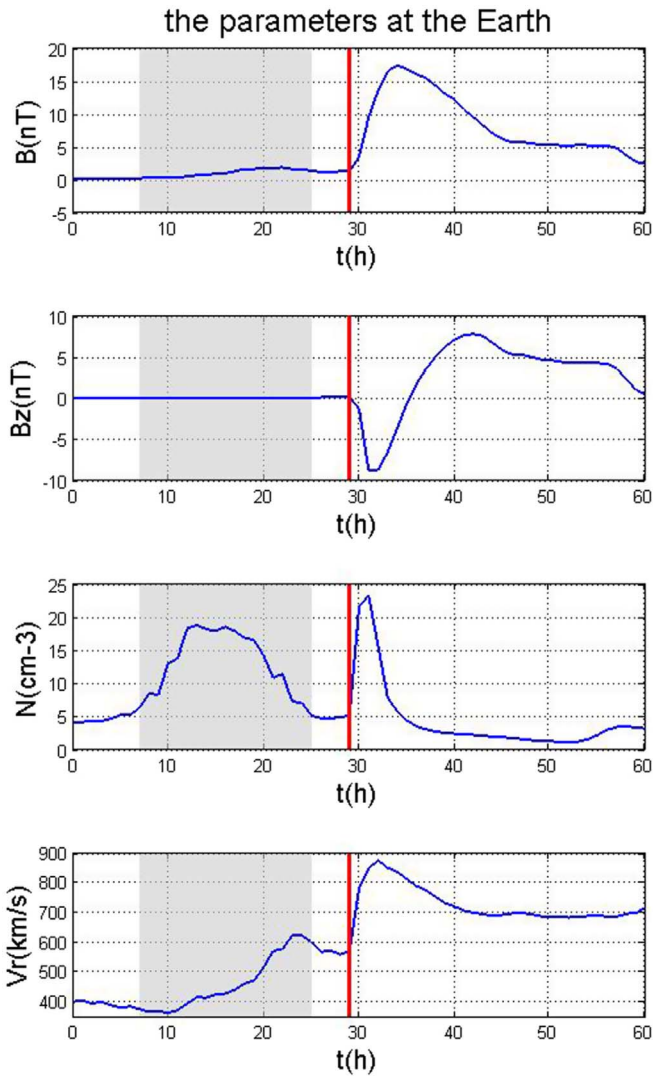


Figure 6. Profiles of plasma parameters at Earth for 60 hr after the launch. The red line indicates the time when the CME arrives at Earth; the gray areas indicate the time when Earth is passing through the CIR.

i.e., 1.15×10^8 km when the propagation time is about 35 hr, i.e., 1.26×10^5 s. So the average radial speed of the CME is calculated to be about 910 km s^{-1} . Then the deflection angle at 35 hr can be estimated to be about 5.66° by Equation (23). To compare with the deflection angle in our simulation directly, this result is also added to Figures 8(a) and (b) (as red dashed lines).

As can be seen from the above, the modeled deflection angle of a fast CME propagating freely to 1 au in the background solar wind is about 5° , which is consistent with the DIPS model. When the same CME interacts with CIR, the deflection angle increases to more than 10° for the same propagation distance. The main difference in the CME propagation process between the above two cases is whether there is a significant interaction with CIR. And we can see from the density image in Figure 5 that the interaction between CME and CIR is so intense that even the shape of CIR is seriously affected. Therefore, the interaction with CIR should play an important role in the increase of the deflection angle of CME.

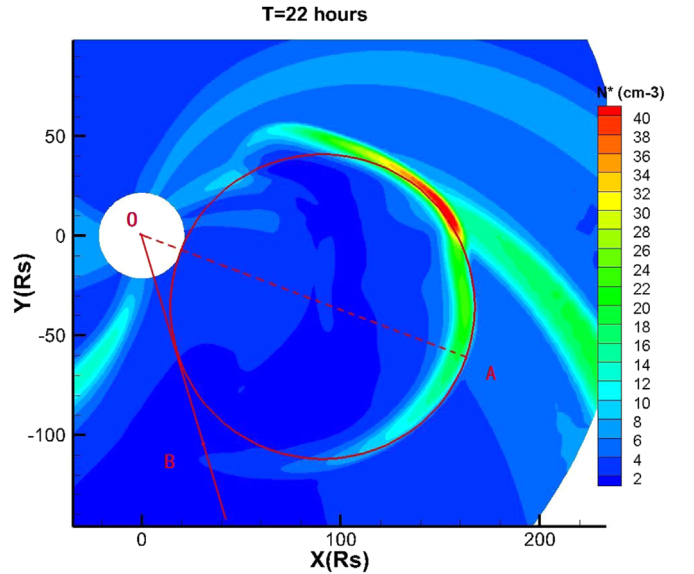


Figure 7. Schematic of the CME circle, which is shown as a red circle in the figure; O is the location of the Sun; A is the point of CME front we defined; B is the easternmost point of the CME.

4. Summary and Discussion

In this work, we have numerically investigated the propagation and deflection of the fast CME in the interplanetary space. Considering whether the CME interacts with the CIR or not, we have analyzed the difference between these two cases, including their deflection angle and trajectory. The CR 2154 is chosen for our study because the interplanetary solar wind configuration has several distinct CIRs and is suitable for our simulation and comparison. A steady-state interplanetary background solar wind is established by a 3D IN-TVD-MHD model first. Then we established a CME initialization model based on the GCS model. Two CMEs based on this model are put into the background for comparison. Their initial geometric and physical parameters are identical; however, their launching locations are different. One of them interacts with CIR during the propagation, while the other does not. Finally, their location, trajectory, and deflection are analyzed.

Our simulation results show that a fast CME propagating in the interplanetary solar wind always deflects to the east. If the CME has an average speed of 910 km s^{-1} , its deflection angle is about 5° when it arrives near the Earth orbit (1 au). If a fast CME with the same initialization parameters interacts with the CIR ahead, it will be deflected to the east too. However, the deflection is more significant compared with the one that propagates freely. When it travels with the same average speed of 910 km s^{-1} , the deflection angle can be over 10° near 1 au. From the comparison between these two cases, we demonstrate that the deflection of the CME is quite different, with different background conditions.

We know that in the corona, the magnetic energy always plays a dominant role in the CME's dynamic process, while in the interplanetary space, the magnetic field is much weaker and the velocity of the CME is much higher, therefore the dynamic energy of the CME is predominant. In our work, the interplanetary propagation of CME is focused, so we tend to look for an explanation for this phenomenon from the view of density and pressure.

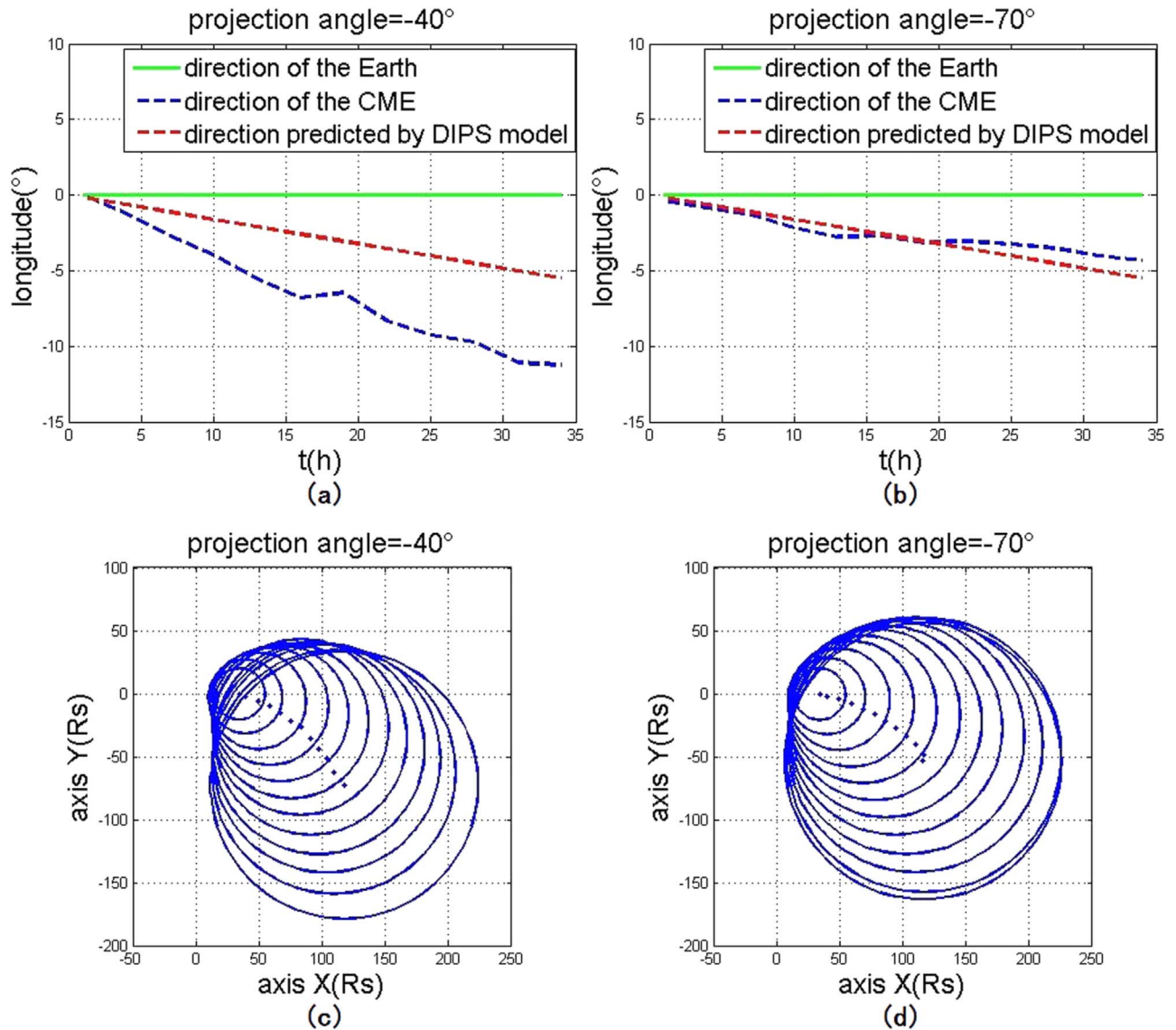


Figure 8. (a) and (c): temporal images of the CME’s deflection angles and the trajectories of the CME circle, respectively, for the case when the CME interacts with the CIR. (b) and (d): images for the case when the CME does not interact with the CIR. (a) and (b) are shown in the heliocentric Earth ecliptic coordinate system, while (c) and (d) are in rotating coordinates. The green line is the longitude of the Earth; the blue dashed line is the CME direction of our simulation; the red dashed line is the CME direction predicted by DIPS model. The time interval for each CME circle in (c) and (d) is 3 hr.

From the view of the DIPS model, the deflection angle was determined by the difference between the CME velocity and background solar wind velocity. However, the essence of this view is that the velocity difference would make the plasma accumulate on one side of the CME and then causes the total pressure on this side to rise. And it is this imbalance of pressure that causes CME to deflect. Similar views have been proposed by Wang et al. (2004), and they think that the leading flow would have a “block” effect on the fast CME. So does it in our cases: during the propagation of a fast CME, the interplanetary plasma and magnetic field will accumulate at its west side; the density at the west side will increase as well as the total pressure; the rising pressure at the west causes the CME to deflect eastward. As can be seen clearly in Figures 5(a)–(c), there is a marked increase of density in the region contacted with CIR on the west side of the CME, which is shown in red color in the figure. Compared with other regions in the background solar wind, the CIR has higher density and lower speed. This makes the mass accumulation more, and causes the

pressure to rise more in this region. The more pressure rises at the west side, the greater the deflection. Thus, the deflection angle is larger when the CME interacts with CIR.

As mentioned above, our simulation mainly focuses on the propagation and deflection of CME in the interplanetary, so the inner boundary, where the CME is launched, is located at 0.1 au. Thus, the GCS model cannot connect directly to the Sun. Two magnetic field legs of the flux-rope structure, which are supposed to come from the solar surface, are cut off by the inner boundary. After we initialize the CME model, it will propagate in the background solar wind, where the magnetic field is going outward in a single direction. Because of the absence of two legs connected to the solar surface, it is hard to keep such a curved shape, which is like a hollow crossant. The whole magnetic field structure of the model will soon be influenced by the background magnetic field configuration. Although the structure of the twisted magnetic field could be retained, the overall shape of the flux-rope will gradually be straightened by the background magnetic field. This may lead

to the partial distortion of the CME's magnetic field configuration.

In our future work, the corona regions will also be included in the research. The interaction between CME and other structures in the corona, mainly the magnetic field structure will be simulated, and the deflection of CME in the corona region will be studied. Moreover, we will try to simulate the real CME deflection event with the influence of CIR structure by using more observational data collected by, e.g., from *Parker Solar Probe* and *Solar Orbiter*, in the future.

The synoptic magnetogram data in this work are obtained from the Global Oscillation Network Group (GONG) of the National Solar Observatory. The numerical calculation has been completed on TianHe-1 (A) at the National Super-computer Center in Tianjin, China. We acknowledge their use. This work is jointly supported by grants from the National Natural Science Foundation of China (41474152, 41531073, 41731067, 41774184, and 41974202) and the Specialized Research Fund for State Key Laboratories. F.S. is also supported by the National Program for Support of Top-notch Young Professionals.

ORCID iDs

Fang Shen  <https://orcid.org/0000-0002-4935-6679>

References

- Arge, C. N., Odstrcil, D., Pizzo, V. R., & Mayer, L. 2003, Solar Wind Ten, in AIP Conf. Ser. 679, ed. M. Velli et al. (Melville, NY: AIP), 190
- Chané, E., Jacobs, C., van der Holst, B., Poedts, S., & Kimpe, D. 2005, *A&A*, 432, 331
- Chané, E., van der Holst, B., Jacobs, C., Poedts, S., & Kimpe, D. 2006, *A&A*, 447, 727
- Dasso, S., Mandrini, C., Demoulin, P., & Luoni, M. 2006, *A&A*, 455, 349
- Feng, X., Yang, L., Xiang, C., et al. 2010, *ApJ*, 723, 300
- Gibson, S., & Low, C. B. 1998, *ApJ*, 493, 460
- Gopalswamy, N., Yashiro, S., Kaiser, M., Howard, R., & Bougeret, A. 2001, *ApJL*, 548, L91
- Gosling, J., Bame, J. S., McComas, D., & Phillips, L. J. 1990, *GeoRL*, 17, 901
- Gosling, J., & Pizzo, V. 1999, *SSRv*, 89, 21
- Gui, B., Shen, C., Wang, Y., et al. 2011, *SoPh*, 271, 111
- Howard, R. A., Michels, D. J., Sheeley, N. R., Jr., & Koomen, M. J. 1982, *ApJ*, 263, 101
- Kay, C., Opher, M., Colaninno, R., & Vourlidas, A. 2016, *ApJ*, 827, 70
- Kay, C., Opher, M., & Evans, R. 2015, *ApJ*, 805, 168
- Liu, Y., Thernisien, A., Luhmann, J., et al. 2010, *ApJ*, 722, 1762
- Lugaz, N., Farrugia, C., Davies, J., et al. 2012, *ApJ*, 759, 68
- Lugaz, N. I., Manchester, W. B., IV, & Gombosi, T. I. A. 2005, *ApJ*, 634, 651
- Lundquist, S. 1951, *PhRv*, 83, 307
- Lynch, B., Li, Y., Thernisien, A., et al. 2010, *JGRA*, 115, 7106
- Manchester, W., Kilpua, E., Liu, Y., et al. 2017, *SSRv*, 212, 1159
- Manchester, W. B., Gombosi, T., Roussev, I., et al. 2004a, *JGR*, 109, A01102
- Manchester, W. B., Gombosi, T., Roussev, I., et al. 2004b, *JGR*, 109, A02107
- Manchester, W. B., Kozyra, J., Lepri, S., & Lavraud, B. 2014a, *JGRA*, 119, 5449
- Manchester, W. B., van der Holst, B., & Lavraud, B. 2014b, *PPCF*, 56, 064006
- Odstrcil, D., & Pizzo, V. 1999, *JGR*, 104, 28225
- Patsourakos, S., Vourlidas, A., & Kliem, B. 2010, *A&A*, 522, A100
- Poomvises, W., Zhang, J., & Olmedo, A. 2010, *ApJL*, 717, L159
- Shen, C., Wang, Y., Gui, B., Ye, P., & Wang, S. 2011a, *SoPh*, 269, 389
- Shen, C., Wang, Y., Wang, S., et al. 2012a, *NatPh*, 8, 923
- Shen, F., Feng, X., Wang, Y., et al. 2011b, *JGRA*, 116, A09103
- Shen, F., Feng, X., Wu, S., Xiang, C., & Song, B. W. 2011c, *JGRA*, 116, 4102
- Shen, F., Shen, C., Wang, Y., Feng, X., & Xiang, C. 2013, *GeoRL*, 40, 1457
- Shen, F., Shen, C., Zhang, J., et al. 2014, *JGRA*, 119, 7128
- Shen, F., Wu, S., Feng, X., & Wu, C. C. 2012b, *JGRA*, 117, A11101
- Shen, F., Yang, Z., Zhang, J., Wei, W., & Feng, X. 2018, *ApJ*, 866, 18
- Shiota, D., & Kataoka, R. 2016, *SpWea*, 14, 56
- Thernisien, A. 2011, *ApJS*, 194, 33
- Thernisien, A., Howard, R., & Vourlidas, A. 2006, *ApJ*, 652, 763
- Thernisien, A., Vourlidas, A., & Howard, R. 2009, *SoPh*, 256, 111
- Vandas, M., Fischer, S., Dryer, M., Smith, Z., & Detman, T. 1998, *JGR*, 103, 23717
- Vandas, M., Fischer, S., Pelant, P., et al. 1997, *JGR*, 102, 24183
- Vandas, M., Odstrcil, D., & Watari, S. 2002, *JGRA*, 107, 1236
- Wang, Y., Chen, C., Gui, B., et al. 2011, *JGRA*, 116, 4104
- Wang, Y., Shen, C., Wang, S., & Ye, P. 2004, *SoPh*, 222, 329
- Wang, Y., Wang, B., Shen, C., Shen, F., & Lugaz, N. 2014, *JGRA*, 119, 5117
- Xiong, M., Zheng, H., & Wang, S. 2009, *JGRA*, 114, A11101
- Xiong, M., Zheng, H., Wu, S., Wang, Y., & Wang, S. 2007, *JGRA*, 112, A11103
- Zhou, Y., & Feng, X. 2013, *JGRA*, 118, 6007
- Zhou, Y., & Feng, X. 2017, *JGRA*, 122, 1451